S.J.P.Pamela, G.T.A.Huijsmans, A.Bhole, B.Nkonga, M.Hoelzl, I.Krebs

Extended Full-MHD Simulation of Non-linear Instabilities in Tokamak Plasmas

Extended Full-MHD Simulation of Non-linear Instabilities in Tokamak Plasmas

S.J.P.Pamela, G.T.A.Huijsmans, A.Bhole, B.Nkonga, M.Hoelzl, I.Krebs

Extended Full-MHD Simulation of Non-linear Instabilities in Tokamak Plasmas

S.J.P.Pamela[1], A.Bhole[2,3], G.T.A.Huijsmans[4,5], B.Nkonga[2,3], M.Hoelzl[6], I.Krebs[7], E.Strumberger[6] and the JOREK team[8].

[*] *EUROfusion Consortium, JET, Culham Science Centre, Abingdon, OX14 3DB, UK.*
[1] *CCFE, Culham Science Centre, Abingdon, Oxon, OX14 3DB, UK.*
[2] *Universite Cote d'Azur, J.A.D, UMR CNRS UNS, Nice, France.*
[3] *CASTOR Team, Inria Sophia Antipolis, Nice, France.*
[4] *CEA, IRFM, F-13108 Saint-Paul-lez-Durance, France.*
[5] *Eindhoven University of Technology, Eindhoven, The Netherlands.*
[6] *Max-Planck Institute for Plasma Physics, Garching, Germany.*
[7] *DIFFER - Dutch Institute for Fundamental Energy Research, De Zaale 20, 5612 AJ Eindhoven, the Netherlands.*
[8] *See [https://www.jorek.eu] for the present list of team members.*

Abstract

Non-linear MHD simulations play an essential role in active research and understanding of tokamak plasmas for the realisation of a fusion power plant. The development of MHD codes like JOREK is a key aspect of this research effort. In this paper, we present a fully operational full-MHD model in JOREK, a significant advancement from the reduced-MHD model used for previous studies. The model is presented in detail, and benchmarks are performed using both linear and non-linear simulations, including comparisons between the new full-MHD model of JOREK and the previously extensively studied reduced-MHD model, as well as results from the linear full-MHD code CASTOR3D. It is shown that this new JOREK full-MHD model is numerically and physically reliable, even without the use of numerical stabilisation methods. Non-linear modelling results of typical tokamak instabilities are presented, including disruption and ELM physics, most relevant to current open issues concerning future tokamaks like ITER and DEMO.

1 Introduction

Industrial electricity production using nuclear fusion power would greatly contribute to the reduction of greenhouse gas emissions and of long-lived radioactive nuclear waste, while providing electricity to society without the limit of an exhaustible natural resource. A favorable candidate for industrial fusion reactors is the tokamak device. Tokamaks use a helical magnetic field that winds itself around a toroidal vacuum chamber. The periodic nature of the torus ensures that charged particles, which approximately follow magnetic field lines, are not lost at the end of open field lines like in linear plasma devices. However, this periodicity can be subject to resonance and instabilities. Large-scale instabilities typically involve both the plasma and the magnetic field, and are often studied in the fluid picture using magnetohydrodynamics (MHD).

There is a wide variety of MHD instabilities in tokamak plasmas, some of which can reduce or limit the operational capabilities of the machine. Edge-Localised-Modes (ELMs) are instabilities that eject plasma from the confined region onto the material surfaces of the first wall of the machine; these instabilities can lead to large heat-fluxes that may reduce the life-time of the material surfaces [1–4]. Toroidal Alfven Eigenmodes (TAEs) can be excited by the 3.5MeV alpha-particles born from fusion reactions; these can significantly limit the plasma pressure, and are a concern for future reactors where the burning plasma will produce a large amount of alpha-particles [5–8]. Global MHD instabilities, during which the entire plasma is affected, can lead to disruptions; during such events the kinetic and magnetic energy of the plasma can be transferred to the wall, leading to material heat-fluxes and/or wall-currents that can damage the machine and its structure [9–14]. In order to study, understand and predict these instabilities, non-linear MHD simulations are performed using numerical codes like JOREK [15, 16], M3D-C1 [17, 18], NIMROD [19, 20], XTOR [21], BOUT++ [22, 23], MEGA [24, 25], HALO [7] and many others.

Previous studies of MHD instabilities with the JOREK code relied on a reduction of the full-MHD system. This reduction assumes that the toroidal magnetic field is constant in time, and that the perpendicular velocity (perpendicular with respect to the magnetic field) is approximately poloidal [26, 27]. While the latter assumption is mostly kept for simplicity in formulating the equations, the former leads to physical simplifications of the representation of tokamak dynamics. In particular, fixing the toroidal magnetic field in time removes some of the waves from the model, commonly referred to as fast magneto-sonic waves. These fast-waves propagate by compressing the magnetic field and the fluid in the direction perpendicular to the magnetic field. They are inherently stable with a wave-length and amplitude much smaller than the marco-instabilities of interest in tokamak devices. However these waves can pollute and restrict the solution of numerical codes, and modelling codes often rely on distinct formulations or numerical stabilisation to avoid numerical issues with these fast waves. Therefore, reduced-MHD is a powerful model in the sense that fast-waves are entirely removed from the system, and it is clearly sufficient to describe the non-linear dynamics of most tokamak instabilities. However, it is already widely acknowledged that some tokamak instabilities, particularly internal kink instabilities, cannot properly be captured by

reduced-MHD [28], and so including both the full-MHD and the reduced-MHD models in JOREK is absolutely necessary.

In this paper, we present the full-MHD model implemented in JOREK, and applied to linear and non-linear instabilities. A first implementation of the full-MHD model had already been presented in [29]. Unfortunately, this initial implementation suffered numerical issues that restricted simulations to low-beta instabilities only. All numerical issues have now been resolved, such that modelling of all instabilities of interest is now possible. Section-2 of the paper presents the physics model of the full-MHD system. Section-3 addresses the linear benchmark of the model for several types of MHD instabilities, and how it compares to the reduced-MHD model. Section-4 demonstrates the capability of the code to deal with large non-linear instabilities like ELMs and disruptions. Finally Section-5 summarises the work and lays out the further improvements required for future studies of tokamak instabilities.

2 The full-MHD model

In this section, we describe the essential physical and numerical ingredients of the full-MHD model implemented in JOREK, including visco-resistive and diffusive effects, sources, diamagnetic rotation and neoclassical friction, boundary conditions and normalisation.

Basis of the full-MHD formulation

In order to ensure that the magnetic field satisfies Gauss's law $\nabla \cdot \vec{B} = 0$, we defined the magnetic field as

$$\vec{B} \;=\; \frac{F}{R}\vec{e}_\phi \;+\; \nabla \times \vec{A} \tag{1}$$

where $\vec{A}$ is the magnetic vector potential, and $F = F(\psi)$ is a toroidally axisymmetric equilibrium function, defined to satisfy the initial Grad-Shafranov equilibrium (ψ is the poloidal magnetic flux). F is constant in time, and thus the evolution of the toroidal magnetic field is determined by $\vec{A}$ alone. Note: this differs from reduced MHD definition of $B_\phi = F_0/R$, where F_0 is constant both in space and time. It should be noted that this formulation of the magnetic field ensure $\nabla \cdot \vec{B} = 0$ exactly, without any approximation. The other variables of the system are the velocity vector field $\vec{v}$, the mass density ρ, and the temperature T. The resistive MHD model is described by

$$\frac{\partial \vec{A}}{\partial t} \;=\; \vec{v} \times \vec{B} \;-\; \eta \vec{J} \;-\; \nabla \Phi, \tag{2}$$

$$\rho \frac{\partial \vec{v}}{\partial t} \;=\; -\rho \vec{v} \cdot \nabla \vec{v} \;+\; \vec{J} \times \vec{B} \;-\; \nabla p, \tag{3}$$

$$\frac{\partial \rho}{\partial t} \;=\; -\nabla \cdot \left(\rho \vec{v} \right), \tag{4}$$

$$\frac{\partial p}{\partial t} \;=\; -\vec{v} \cdot \nabla p \;-\; \gamma p \nabla \cdot \vec{v} \tag{5}$$

where η is the resistivity, and Φ is the electric potential obtained from uncurling Faraday's law $\nabla \times \left[\partial_t \vec{A} = -\vec{E} \right]$. The current is defined as $\vec{J} = \nabla \times \vec{B}$, and the total pressure as $p = \rho T$. The

ratio of specific heats γ is taken to be that of a monatomic gas, $\frac{5}{3}$. More details about normalisation of the equations are included at the end in this section.

Choice of gauge

Since the magnetic field is invariant with respect to the transformation $\vec{A} \to \vec{A} + \nabla \Psi$ (for any scalar function Ψ), a convenient choice is to use Weyl's gauge, where Ψ is chosen such that

$$\Phi = -\partial_t \Psi, \tag{6}$$

which simplifies the induction equation (2) to give

$$\frac{\partial \vec{A}}{\partial t} \;=\; \vec{v} \times \vec{B} \;-\; \eta \vec{J} \tag{7}$$

In practice, this means that if an external electric field is applied to the plasma, the magnetic vector potential will shift in time (even in stationary equilibrium state).

Diffusion coefficients and sources

In addition to the resistivity η, physical diffusion coefficients are also included for all other variables. The perpendicular diffusion of density and temperature need to be balanced in order to retain the initial Grad-Shafranov equilibrium, thus sources are also introduced for density and temperature. The visco-resistive MHD equations are thus written as

$$\frac{\partial \vec{A}}{\partial t} \;=\; \vec{v} \times \vec{B} \;-\; \eta \left(\vec{J} - \vec{S}_j \right), \tag{8}$$

$$\rho \frac{\partial \vec{v}}{\partial t} \;=\; -\rho \vec{v} \cdot \nabla \vec{v} \;+\; \vec{J} \times \vec{B} \;-\; \nabla p \;+\; \mu \nabla^2 \vec{v} \;-\; \Gamma_\rho \vec{v}, \tag{9}$$

$$\frac{\partial \rho}{\partial t} \;=\; -\nabla \cdot (\rho \vec{v}) \;+\; \nabla \cdot \left(D_\perp \nabla_\perp \rho + D_\parallel \nabla_\parallel \rho \right) \;+\; S_\rho, \tag{10}$$

$$\frac{\partial p}{\partial t} \;=\; -\vec{v} \cdot \nabla p \;-\; \gamma p \nabla \cdot \vec{v} \;+\; \nabla \cdot \left(\kappa_\perp \nabla_\perp T + \kappa_\parallel \nabla_\parallel T \right) \;+\; S_T \tag{11}$$

where the particle diffusion and the thermal conductivity have been split into perpendicular and parallel components, $D_\perp$ and $D_\parallel$, and $\kappa_\perp$ and $\kappa_\parallel$ respectively. The parallel and perpendicular gradient operators are defined as

$$\nabla_\parallel \;=\; \frac{1}{|B|^2} \vec{B} \left[\vec{B} \cdot \nabla \right],$$
$$\nabla_\perp \;=\; \nabla - \nabla_\parallel.$$

The current source $\vec{S}_j$ keeps the current profile steady for long simulations. $\vec{S}_j$ also includes the bootstrap current source which evolves as a function of the pressure gradient, and is particularly essential for cyclic instabilities like ELMs. Instead of a current source $\vec{S}_j$, it is also possible to use a loop voltage as boundary conditions. The particle source S_ρ and the heating source S_T, which are generally used only to balance against axisymmetric equilibrium diffusive terms, can also be used

for other purposes. A good example is to use a time-evolving particle source S_ρ to model pellet injections. In Section-4, S_ρ is used to mimic a massive-gas-injection (MGI) disruption. Note that since the continuity equation-(10) has been used in the derivation of the momentum equation-(9), the particle source term must also be kept there. If ignored, large particle sources like pellets would also lead to an artificial injection of momentum. The diffusive terms from the continuity equation, although generally much smaller, are also kept in the momentum equation. This is represented by the last term in equation-(9), where $\Gamma_\rho = \nabla \cdot \left(D_\perp \nabla_\perp \rho + D_\parallel \nabla_\parallel \rho \right) + S_\rho$.

The physical diffusive coefficients are non-constant. Radial profiles for $D_\perp$ and $\kappa_\perp$ can be used to mimic various levels of cross-field kinetic turbulent transport, which cannot be described by MHD. This is important for situations like the H-mode, where cross-field turbulent transport is known to be strongly reduced in the pedestal region, at the plasma edge. In simulations of ELMs, for example, a radial drop in $D_\perp$ and $\kappa_\perp$ is localised at the pedestal region to sustain the large pedestal pressure gradient of pre-ELM conditions. The viscosity and resistivity both have a Spitzer-like dependence on temperature, $\eta = \eta_0 T^{-3/2}$ and $\mu = \mu_0 T^{-3/2}$ respectively, where η_0 and μ_0 are the values of resistivity and viscosity on the magnetic axis. The parallel particle diffusion is typically kept to zero, while the parallel thermal conductivity is formulated using the Braginskii model $\kappa_\parallel = \kappa_0 T^{5/2}$, for which κ_0 has well-defined physical amplitudes for ion and electron temperatures. Since the present model only includes a single temperature, the value of κ_0 is typically chosen to be the average of ion and electron temperature coefficients.

At present, numerical (or hyper-) diffusion is not needed in the model for any equation, even with strongly non-linear cases, as will be shown in Section-4. In future works, it may be adequate to introduce hyper-resistivity for physical reasons [13].

Extended MHD

For many tokamak applications, additional non-ideal effects are necessary to address certain physical properties of non-linear MHD instabilities. In particular, rotation effects can have a significant impact on the linear stability and the non-linear dynamic of MHD instabilities. The toroidal momentum induced by the Neutral-Beam Injection (NBI) can be significant, particularly in small and medium-size spherical tokamaks like COMPASS, NSTX-U and MAST-U; although this rotation becomes marginal in larger devices like ITER [30]. The diamagnetic rotation [31] has a damping effect on the stability of high toroidal mode numbers, and plays a major role in the dynamics of quasi-periodic relaxations, like ELMs and neoclassical tearing modes (NTMs) [32–37]. Finally, neoclassical poloidal rotation also plays an important role in the rotation of precursor modes in ELMy H-mode simulations [38].

The full system of extended MHD equations, including diffusion, sources, and rotation effects,

is described by

$$\frac{\partial \vec{A}}{\partial t} = \vec{v} \times \vec{B} + \frac{m_i}{2e\rho}\nabla_\parallel p - \eta\left(\vec{J} - \vec{S}_j\right), \tag{12}$$

$$\rho\frac{\partial \vec{v}}{\partial t} = -\rho\left(\vec{v} + \vec{v}_{i*}\right)\cdot\nabla\vec{v} + \vec{J}\times\vec{B} - \nabla p + \mu\nabla^2\left(\vec{v} - S_{NBI}\right) + \nabla\cdot\Pi_{neo} - \Gamma_\rho\vec{v} \tag{13}$$

$$\frac{\partial \rho}{\partial t} = -\nabla\cdot(\rho\vec{v}) - \vec{v}_{i*}\cdot\nabla\rho + \nabla\cdot\left(D_\perp\nabla_\perp\rho + D_\parallel\nabla_\parallel\rho\right) + S_\rho, \tag{14}$$

$$\frac{\partial p}{\partial t} = -\vec{v}\cdot\nabla p - \gamma p\nabla\cdot\vec{v} + \nabla\cdot\left(\kappa_\perp\nabla_\perp T + \kappa_\parallel\nabla_\parallel T\right) + S_T \tag{15}$$

where the ion diamagnetic velocity and the neoclassical poloidal friction tensor are defined respectively as

$$\vec{v}_{i*} = \frac{m_i}{2e\rho B^2}\vec{B}\times\nabla p. \tag{16}$$

$$\nabla\cdot\Pi_{neo} = \mu_{neo}\rho\frac{B^2}{B_\theta^2}\left(v_\theta - v_{neo}\right)\vec{e}_\theta \tag{17}$$

$$v_{neo} = -\frac{k_i m_i}{2e B_\theta}\left(\nabla T\times\vec{B}\right)\cdot\vec{e}_\theta \tag{18}$$

with m_i and e being the ion mass and charge respectively, k_i being the neoclassical heat diffusivity, and $\vec{e}_\theta = \vec{B}_\theta/|\vec{B}_\theta|$ being the unit vector along the poloidal magnetic field $\vec{B}_\theta = B_R\vec{e}_R + B_Z\vec{e}_Z$. The poloidal velocity is thus defined as $v_\theta = (\vec{v} + \vec{v}_{i*})\cdot\vec{e}_\theta$. Note that the factor 2 in the definition of the diamagnetic and neoclassical velocities comes from the assumption that, with a single total temperature T, the ion pressure is assumed to be simply $p_i = p/2$.

Note that the diamagnetic effects have been implemented taking into account the incompressibility of the diamagnetic flow, the gyro-viscous cancellation, and the gyro-viscous heat-flux cancellation, which eliminates several diamagnetic terms in the momentum and energy equations [35, 36]. This diamagnetic cancellation is the common form which assumes a constant magnetic field, not the full (more complex) form where the cancellation involves the magnetization velocity instead of the diamagnetic velocity [39]. The diamagnetic term in the induction equation-(12) is obtained using the standard drift ordering, which we resume here for clarity, starting from the extended Ohm's law for electrons [35]:

$$\vec{E} = -\vec{v}_e\times\vec{B} - \frac{m_i}{e\rho}\nabla p_e + \eta\vec{J} \tag{19}$$

where the electron velocity can be expressed as

$$\begin{aligned}\vec{v}_e &= -\frac{m_i}{e\rho}\vec{J} + \vec{v}_i \\ &= -\frac{m_i}{e\rho}\vec{J} + \vec{v} + \vec{v}_{i,*} \\ &= -\frac{m_i}{e\rho}\vec{J} + \vec{v} + \frac{m_i}{e\rho B^2}\vec{B}\times\nabla p_i\end{aligned}$$

which can be substituted into equation-(19) to be expanded as

$$\vec{E} = -\vec{v} \times \vec{B} + \frac{m_i}{e\rho}\vec{J} \times \vec{B} - \frac{m_i}{e\rho B^2}(\vec{B} \times \nabla p_i) \times \vec{B} - \frac{m_i}{e\rho}\nabla p_e + \eta\vec{J}$$

$$= -\vec{v} \times \vec{B} + \frac{m_i}{e\rho}\vec{J} \times \vec{B} - \frac{m_i}{e\rho}\nabla_\perp p_i - \frac{m_i}{e\rho}\nabla_\perp p_e - \frac{m_i}{e\rho}\nabla_\parallel p_e + \eta\vec{J}$$

$$= -\vec{v} \times \vec{B} + \frac{m_i}{e\rho}\left(\vec{J} \times \vec{B} - \nabla_\perp p\right) - \frac{m_i}{e\rho}\nabla_\parallel p_e + \eta\vec{J}$$

In the drift ordering approximation, the perpendicular force-balance $\frac{m_i}{e\rho}\left(\vec{J} \times \vec{B} - \nabla_\perp p\right)$ is neglected, which is a manner of neglecting the Hall effects. Thus, the final formulation of Ohm's law can be written as

$$\vec{E} = -\vec{v} \times \vec{B} - \frac{m_i}{e\rho}\nabla_\parallel p_e + \eta\vec{J} \qquad (20)$$

This is the form used in equation-(12), assuming that $p_e = p/2$.

Projection and coordinate system

The momentum and induction equations each need to be projected in order to obtain individual equations for each of their vector-field components. Although the projection could simply be made along the orthogonal cylindrical basis vectors $(\vec{e}_R, \vec{e}_Z, \vec{e}_\phi)$, this is numerically not the most stable choice, particularly for the momentum equation.

The magnetic vector potential, the velocity field and the magnetic field are decomposed as

$$\vec{A} = A_R \vec{e}_R + A_Z \vec{e}_Z + \frac{1}{R}A_\phi \vec{e}_\phi \qquad (21)$$

$$\vec{v} = V_R \vec{e}_R + V_Z \vec{e}_Z + V_\phi \vec{e}_\phi \qquad (22)$$

$$\vec{B} = B_R \vec{e}_R + B_Z \vec{e}_Z + B_\phi \vec{e}_\phi \qquad (23)$$

which means that the toroidally axisymmetric component of A_ϕ is equivalent to the magnetic poloidal flux ψ, and the toroidal components V_ϕ and B_ϕ are the actual physical components of the velocity and magnetic field respectively. Note that if an electric field is present (for example if a loop voltage is used as boundary conditions), then A_ϕ will shift rigidly with time, but the normalised scalar ψ_n will not change (assuming the equilibrium is stationary).

While the induction equation is simply projected along the vectors $(\vec{e}_R, \vec{e}_Z, \vec{e}_\phi)$, the momentum equation is projected along the vectors $(\vec{e}_R, \vec{e}_Z, \vec{B})$. As noted in [29], this choice of projection is essential for the numerical stability of the model. By removing the $\vec{J} \times \vec{B}$ term in the equation for V_ϕ, the $\vec{B}$ projection is thought to remove unnecessary fast-waves components that pollute the solution otherwise. In practice, it was found that projecting the momentum equation in the toroidal direction $\vec{e}_\phi$, instead of $\vec{B}$, for the V_ϕ equation, renders the model entirely unusable, with simulations typically exploding numerically after a few time steps.

Weak formulation

As described in previous papers [16, 40], JOREK uses a weak formulation of the equations, where spatial integration is used to construct the linearised system to be solved. For example, the weak

formulation of a (simplified) continuity equation would be

$$\int \zeta \frac{\partial \rho}{\partial t} dV \;\; = \;\; - \int \zeta \nabla \cdot (\rho \vec{v}) \, dV \;\; + \;\; \int \zeta \nabla \cdot (D \nabla_\perp \rho) \, dV,$$

where the test function ζ, in this case, is chosen to be the cubic Bezier polynomial functions of the finite-elements used in JOREK. One of the main advantages of the weak formulation is that it allows integration by parts of divergence terms, with

$$\int \left[\zeta \nabla \cdot \vec{F} \right] dV \;\; = \;\; - \int \left[\vec{F} \cdot \nabla \zeta \right] dV \;\; + \;\; \int \left[\nabla \cdot \left(\zeta \vec{F} \right) \right] dV$$
$$= \;\; - \int \left[\vec{F} \cdot \nabla \zeta \right] dV \;\; + \;\; \int_\Omega \left[\zeta \vec{F} \cdot \vec{n} \right] dS$$

where Ω is the surface boundary of the simulation domain, and $\vec{n}$ is the unit normal vector of that surface boundary. This integration-by-parts method allows the removal of all derivatives of the magnetic field, for the $\vec{J} \times \vec{B}$ term in the momentum equation, and for the resistive term in the induction equation, thus removing all second-order derivatives of $\vec{A}$. It also reduces the second-order derivatives of the diffusive terms in the momentum, continuity and energy equations.

The full expansion of each component of the current field $\vec{J} = \nabla \times \nabla \times \vec{A}$ is tedious, and thus the weak form greatly simplifies the formulation of the equations in the code. Most importantly, one of the main outcomes of the weak formulation is that it removes all explicit second derivatives from the equations, which is a significant advantage when using C1-continuous finite-elements like those implemented in JOREK [40], since all terms in the equations are guaranteed to be smoothly represented, thus improving numerical stability. (Note: here C1-, or G1-continuity, means continuity of variables and their first-order derivatives across elements).

Boundary Conditions

There are two types of boundary conditions, depending on whether a boundary surface is aligned to a magnetic flux-surface or not. If a boundary coincides with a flux-surface, then all variables are fixed in time (Dirichlet), although this can be relaxed for the density and temperature. If a boundary intersects magnetic field lines, then a mixture of conditions is applied: Dirichlet condition is enforced for the magnetic vector potential $\vec{A}$, free outflow of density is allowed (Neumann), while Mach-1 and Sheath boundary conditions are applied to velocity and temperature respectively, such that

$$\vec{v}_\parallel \;\; = \;\; \vec{v} \cdot \vec{b} \;\; = \;\; \pm \; c_s \;\; = \;\; \sqrt{\gamma T}, \tag{24}$$
$$nT\vec{v}_\parallel \;\; + \;\; \kappa_\parallel \nabla_\parallel T \;\; = \;\; \gamma_{sh} nT\vec{v}_\parallel. \tag{25}$$

where $\vec{b}$ is the unit vector along the magnetic field $\vec{B}$, $\gamma = 5/3$ is the ratio of specific heats, and γ_{sh} is the ion sheath transmission factor, which is typically taken between 4.5 and 10.0, depending on the ion or electron temperature, and on transient energy fluxes [41].

Normalisation

The normalisation used here is based on the vacuum permeability μ_{vac} and the central density ρ_0, such that the current, the pressure, the density, the velocity and time are normalised, respectively, as

$$
\begin{aligned}
\vec{J} &= \mu_{vac} \ \vec{J}_{SI} \\
p &= \mu_{vac} \ p_{SI} \\
\rho &= \frac{1}{\rho_0} \ \rho_{SI} \\
\vec{v} &= \sqrt{\rho_0 \mu_{vac}} \ \vec{v}_{SI} \\
t &= \frac{1}{\sqrt{\rho_0 \mu_{vac}}} \ t_{SI}
\end{aligned}
$$

This normalisation is similar to the Alfven time normalisation, such that for a deuterium plasma with central particle density $n_o = 6 \times 10^{19} \mathrm{m}^{-3}$, a normalized time unit corresponds to approximately $0.5 \mu \mathrm{s}$. (Note, the notation μ_{vac} was used instead of the more conventional notation μ_0 just to avoid confusion with the amplitude of the dynamic viscosity on axis, $\mu = \mu_0 T^{-3/2}$).

Fast-waves, and numerical stability of non-ideal terms

One of the great advantages of reduced-MHD is that it removes the fast-waves from the system. With the full-MHD model described above, fast-waves can pollute the solution and can lead to numerical noise, even to numerical instabilities in some cases. It was found, in particular, that the ∇R and ∇Z projections of the induction equation, for the variables A_R and A_Z, are particularly sensitive to any modification. In the most challenging cases, like X-point H-mode equilibria, the non-ideal terms (both resistivity and diamagnetic velocity) were found to be numerically very challenging, often leading to short-wave oscillations on the scale of the grid elements. Therefore, an option has been introduced in the code to remove the non-ideal terms for the A_R and A_Z equations. As will be shown in the following sections, in practice this does not affect the physics results of interest here, which are clearly dominated by the toroidal component of the induction equation. However, for future applications, and particularly resistive-wall free-boundary modelling with the STARWALL code [42], this issue may become problematic, and may require numerical stabilisation methods, such as Taylor-Galerkin (TG) or Variational-Multi-Scale (VMS) stabilisation [43, 44]. Nevertheless, with the approximation of neglecting non-ideal effects for the poloidal components of $\vec{A}$, this version of the extended full-MHD model enables accurate simulations of most non-linear MHD tokamak instabilities of interest, with remarkable consistency with previous reduced-MHD results, in the limits where reduced-MHD is expected to be applicable.

3 Comparison of Full-MHD and Reduced-MHD

In this section, we address a series of linear benchmarks for tokamak instabilities, to compare the new full-MHD model against the previously implemented reduced-MHD. Linear benchmarks are

conducted for core MHD instabilities, as well as edge peeling-ballooning instabilities, both in circular and X-point plasmas. A comparison of peeling-ballooning modes is provided for the spherical tokamak MAST, for which it is widely, and wrongly, presumed that reduced-MHD cannot describe ELM and filament physics accurately, even though no geometrical approximation is required for the energy-conservative derivation of reduced-MHD [45, 46].

Linear benchmark for core n=1 modes

The first two linear benchmarks are a low-β $m=n=1$ internal kink mode, and a low-β $m=n=1$ tearing-mode. Both instabilities were studied in previous publications, and they are described here for completeness and clarity. The Grad-Shafranov equilibrium quantities and profiles for these two cases are described in [29].

| (a) | (b) | (c) |
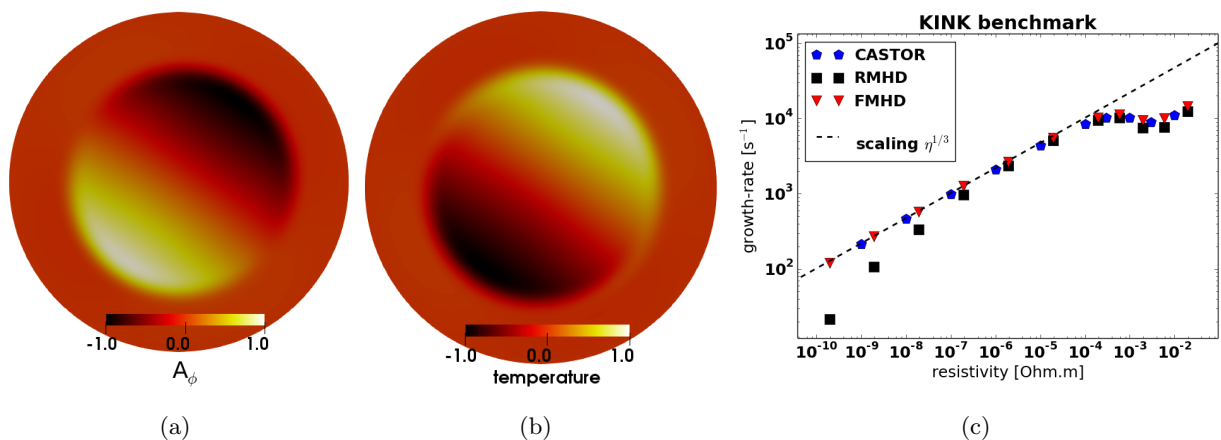
Figure 1:

n=1 internal kink mode benchmark: Poloidal cross-sections of the normalised perturbation of (a) *the toroidal magnetic potential A_ϕ and* (b) *the temperature.* (c) *Comparison of the growth rates of the kink mode with the reduced-MHD model, and with the linear MHD code CASTOR, as a function of resistivity.*

| (a) | (b) | (c) |
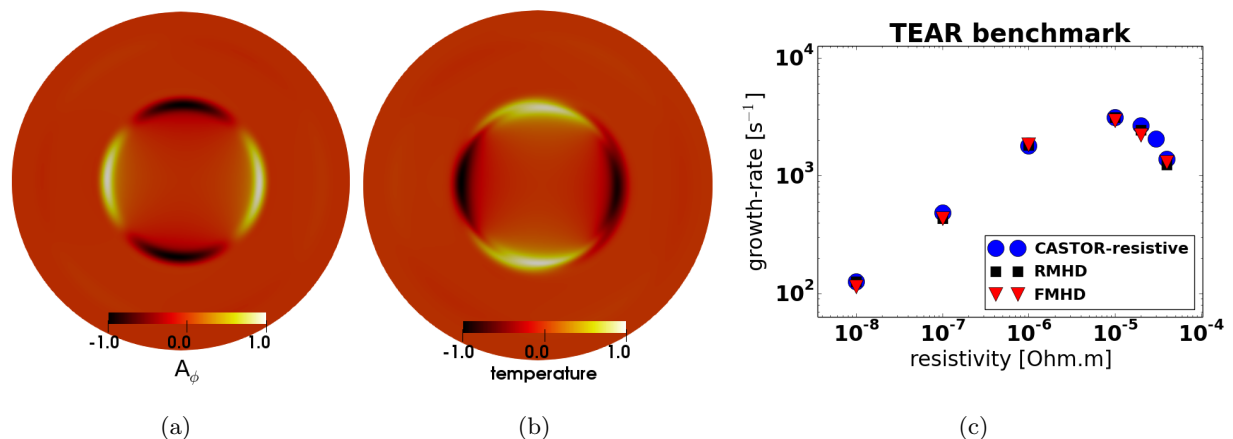
Figure 2:

n=1 tearing mode benchmark: Poloidal cross-sections of the normalised perturbation of (a) *the toroidal magnetic potential A_ϕ and* (b) *the temperature.* (c) *Comparison of the growth rates of the tearing mode with the reduced-MHD model, and with the linear MHD code CASTOR, as a function of resistivity.*

10

Both cases are run for a scan in resistivity. The kink mode is run with resistivity alone (without viscosity, and without particle or thermal diffusion), while the tearing mode is run including all diffusions, with $\mu_0 = 10^{-8}$kg.m^{-1}.s^{-1}, $D_\perp = 0.7$m^2.s^{-1}, and $\kappa_\perp = 1.7 \times 10^{-8}$kg.m^{-1}.s^{-1}.

Figure-1 and Figure-2 show the benchmark of the internal kink mode and the tearing mode respectively, compared to the reduced-MHD model. Poloidal cross-sections of $n = 1$ perturbed quantities are shown for the toroidal magnetic potential A_ϕ and the temperature (for the full-MHD model), and the growth rates of the modes are plotted as a function of resistivity, compared to the reduced-MHD model. A comparison is also made against CASTOR3D, which is also a full-MHD code [47, 48].

Although the agreement between reduced-MHD and full-MHD is reasonable for both cases, the reduced-MHD model starts to deviate from the full-MHD solution at low resistivity for the internal kink mode. This is a typical case where reduced-MHD is expected to fail: for internal kink modes at finite-β [28]. Although this is a low $\beta_N = 0.4\%$ case, reduced-MHD already seems to be affected. At higher-β, the deviation becomes more pronounced.

Where reduced-MHD fails

The internal kink mode at finite-β is a good example to illustrate why full-MHD is absolutely necessary for the modelling of some tokamak instabilities, particularly core MHD, which is highly relevant to disruptions, one of the main focus of current research and experiments. In this benchmark, the results of the linear calculation of a $n = m = 1$ internal kink instability obtained by the reduced-MHD model of JOREK, the full-MHD model of JOREK, and the linear full-MHD code CASTOR3D [47, 48] are compared for different values of β. The equilibrium characteristics of this circular plasma, together with the diffusive parameters used for the simulation, are as follows:

major radius	R_0	10.0 m
minor radius	a	1.0 m
central safety factor	q_{axis}	0.73
location of q=1	$\psi_n|_{q=1}$	0.51
vaccum magnetic field	B_{vac}	1.0 T
total plasma current	I_p	0.3 MA
plasma Beta	β_N	0.0-2.2 %
plasma volume	V	197.0 m^3
resistivity (constant)	η	10^{-6} Ω.m
viscosity (constant)	μ	5.2×10^{-9} kg.m^{-1}.s^{-1}
particle diffusion	$D_\perp$	0.0
perpendicular conductivity	$\kappa_\perp$	0.0
parallel conductivity	$\kappa_\parallel$	0.0

Note that the viscosity here was used only for the JOREK runs, while it is zero for CASTOR3D.

As shown in Figure-3, the full-MHD model of JOREK and CASTOR3D agree well on the linear growth rates, while the reduced-MHD model fails to reproduce these results at finite values of β. This shortcoming of the reduced-MHD model is expected due to the neglect of parallel magnetic field fluctuations [28]. Qualitative differences between the results of the reduced- and full-MHD models are also seen in nonlinear simulations of low mode number core instabilities.
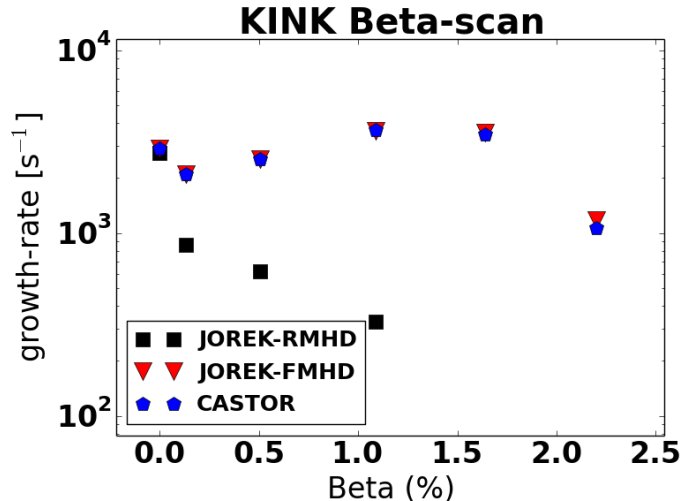
(a)

Figure 3:

n=1 internal kink mode benchmark at finite β: Growth rates of the internal kink mode are compared between the reduced- and full-MHD models of JOREK, together with the linear full-MHD code CASTOR3D. As β is increased, reduced-MHD fails to capture the linear growth of the kink mode, as expected from theory [28].

Peeling-ballooning modes in a circular plasma

The second linear benchmark presented here is the so-called CBM18 case. It is a circular plasma unstable to peeling-ballooning modes, with a $\beta_N \approx 1.3\%$. This case is run for individual toroidal mode numbers between n=1 and n=20. The resistivity for this test-case are set to $\eta_0 = 6\times10^{-6}\Omega.\mathrm{m}$, while all other diffusion coefficients are set to zero.

Figure-4 shows the benchmark of the CBM18 case, when compared to the reduced-MHD model, and also results from MISHKA and CASTOR, which are linear full-MHD code [47, 49, 50]. MISHKA solve the linear incompressible ideal full-MHD model, while CASTOR solves the resistive full-MHD model (also using $\eta_0 = 6\times10^{-6}\Omega.\mathrm{m}$). Poloidal cross-sections of $n = 20$ perturbed quantities are shown for the toroidal magnetic potential A_ϕ and the temperature (for the JOREK full-MHD model), and the growth rates of the modes are plotted as a function of toroidal mode number. The stability threshold of n=4 is well reproduced by the full-MHD model, and the same asymptotic increase of growth rates is observed with both models. The agreement with reduced-MHD and with the linear MHD calculations is reasonable.
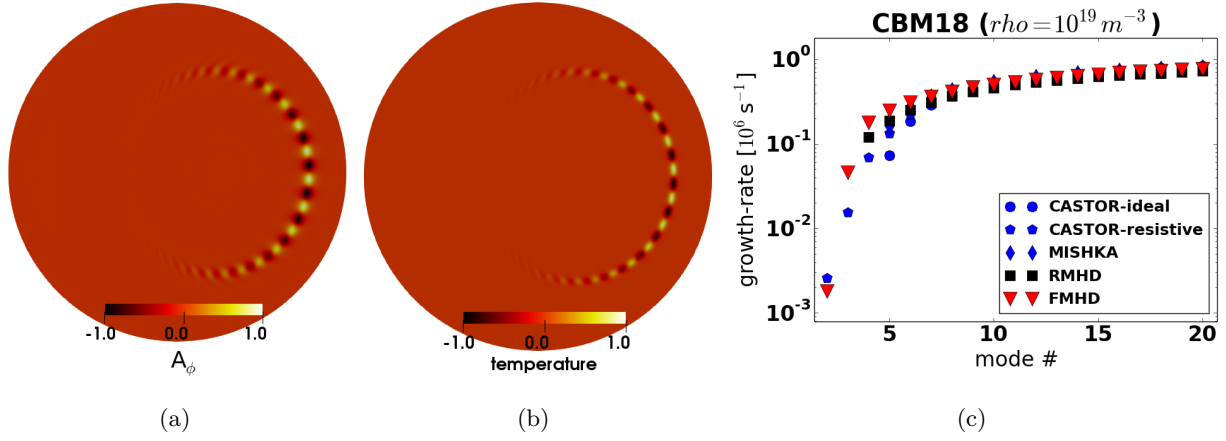
Figure 4:

circular ballooning mode benchmark: Poloidal cross-sections of the normalised perturbation of (a) *the toroidal magnetic potential A_ϕ and* (b) *the temperature.* (c) *Ballooning mode growth rates as a function of toroidal mode number, compared to the JOREK reduced-MHD model, to the MISHKA ideal full-MHD model, and to the CASTOR resistive full-MHD model.*

Peeling-ballooning modes in an X-point plasma

Next, an X-point plasma is run for peeling-ballooning instabilities. This is an artificial equilibrium similar to a JET plasma. It is run using the kinetic stationary background equilibrium flows ($n=0$), together with a single toroidal harmonic, which is changed from $n=1$ up to $n=20$. The equilibrium characteristics, together with the diffusive parameters, are as follows:

major radius	R_0	3.0 m
minor radius	a	0.7 m
elongation	κ	1.7
triangularity	δ	0.0
central safety factor	q_{axis}	0.95
edge safety factor	q_{95}	1.8
vaccum magnetic field	B_{vac}	1.0 T
total plasma current	I_p	0.95 MA
plasma Beta	β_N	2.5 %
plasma volume	V	50.0 m^3
pedestal width	$\Delta\psi_{ped}$	8.0 %
pedestal density	n_e	0.5×10^{20} m^{-3}
pedestal temperature	T_e^{ped}	350 eV
resistivity	η_0	2.7×10^{-6} Ω.m
viscosity	μ_0	3.7×10^{-8} kg.m^{-1}s^{-1}
particle diffusion	$D_\perp$	2.2 m^2.s^{-1}
perpendicular conductivity	$\kappa_\perp$	5.5×10^{-8} kg.m^{-1}.s^{-1}

13

parallel conductivity	$\kappa_{\parallel}$	55.0 `kg.m`$^{-1}$`.s`$^{-1}$

where the $D_{\perp}$ and $\kappa_{\perp}$ values are given on the magnetic axis, with a radial profile that drops by a factor 10 at the top of pedestal. Note, in this list, β_N is defined as $\beta_t/(a.B_t.I_p)$, and $\Delta\psi_{ped}$ is given as a normalised quantity, relative to ψ_n.
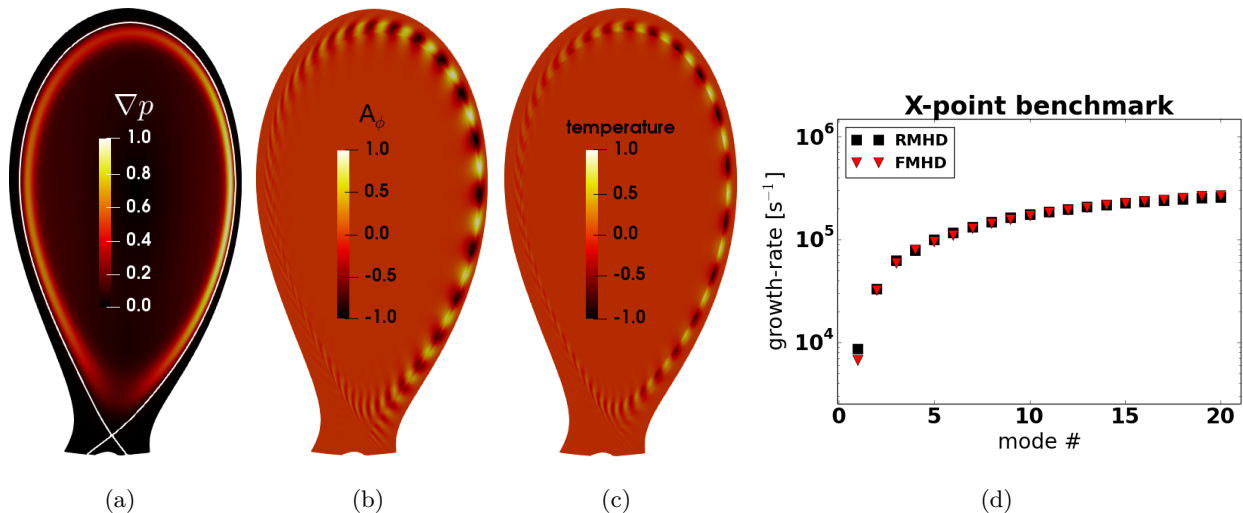
Figure 5:

X-point peeling-ballooning mode benchmark: Poloidal cross-sections of (a) *the normalised equilibrium pressure gradient with the separatrix contour in white,* (b) *the normalised perturbation of the toroidal magnetic potential A_{ϕ},* (c) *the normalised perturbation of the temperature, and* (c) *comparison of the peeling-ballooning mode growth rates with the reduced-MHD model, as a function of toroidal mode number.*

Figure-5 shows the benchmark of the X-point JET-like case, when compared to the reduced-MHD model. Poloidal cross-sections of $n = 20$ perturbed quantities are shown for the toroidal magnetic potential A_{ϕ} and the temperature (for the full-MHD model), together with the initial pedestal pressure gradient. The growth rates of the modes are plotted as a function of toroidal mode number and compared with reduced-MHD. Note that this X-point case is run including the non-static background equilibrium, with stationary flows and Mach-1 boundary conditions, so that this level of agreement with reduced-MHD is excellent.

Peeling-ballooning modes in a spherical tokamak

The next benchmark of interest is the MAST plasma discharge #24763. This case was the subject of previous studies using reduced-MHD [51]. It is typically assumed that reduced-MHD is not adequate to study MHD instabilities in spherical tokamaks. The first derivations by H.R.Strauss [26] relied on a large inverse aspect-ratio assumption to demonstrate the validity of the reduced-MHD ansatz in tokamaks, but it was later demonstrated that the large inverse aspect-ratio is not needed to ensure energy conservation [45, 46]. Nevertheless, this original large inverse aspect-ratio assumption has affected the reputation of the model even until now. Of course, there are instabilities where reduced-MHD fails, like the high-β internal kink mode, but for ELM physics it

seems not to be the case. As such, this benchmark is a validation of reduced-MHD as much as the new full-MHD model.

The MAST discharge #24763 is a nearly symmetrical double X-point equilibrium, with the following characteristics and diffusion coefficients:

central safety factor	q_{axis}	0.58
edge safety factor	q_{95}	4.4
vaccum magnetic field	B_{vac}	0.4 T
total plasma current	I_p	0.85 MA
plasma Beta	β_N	3.0 %
plasma volume	V	8.3 m^3
pedestal width	$\Delta\psi_{ped}$	2.2 %
pedestal density	n_e	0.4×10^{20} m^{-3}
pedestal temperature	T_e^{ped}	220 eV
resistivity	η_0	3.0×10^{-6} Ω.m
viscosity	μ_0	3.4×10^{-8} kg.m^{-1}.s^{-1}
particle diffusion	$D_\perp$	2.4 m^2.s^{-1}
perpendicular conductivity	$\kappa_\perp$	5.0×10^{-8} kg.m^{-1}.s^{-1}
parallel conductivity	$\kappa_\parallel$	500.0 kg.m^{-1}.s^{-1}

where the $D_\perp$ and $\kappa_\perp$ values are given on the magnetic axis, with a radial profile that drops by a factor 10 at the top of pedestal.

(a) (b) (c) (d)
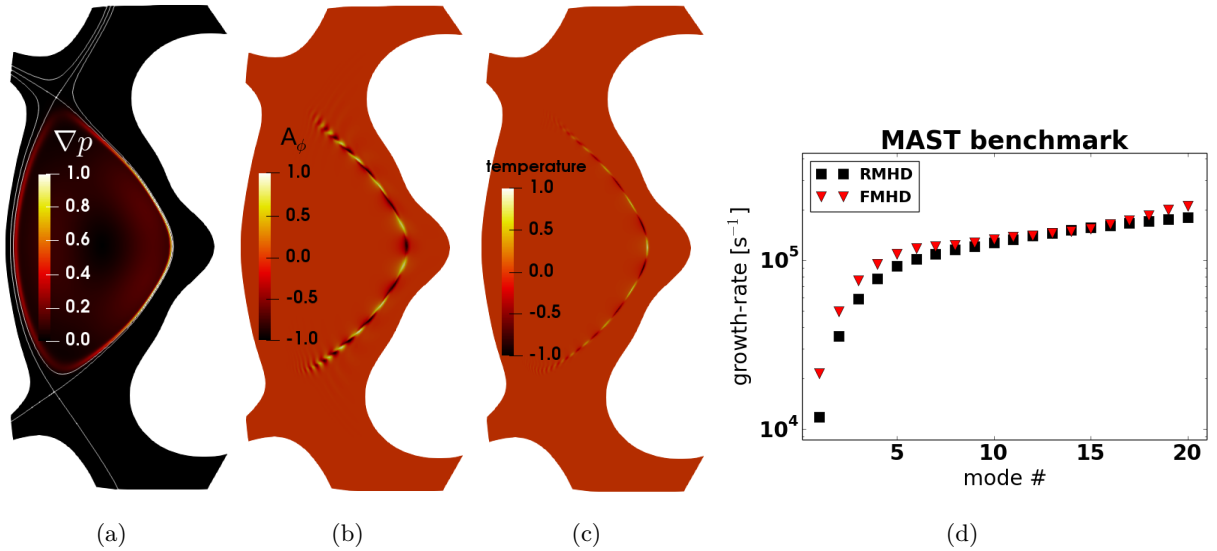
Figure 6:

Spherical tokamak peeling-ballooning mode benchmark, using a MAST double X-point plasma: Poloidal cross-sections of (a) the normalised equilibrium pressure gradient with the two separatrix contours in white, (b) the normalised perturbation of the toroidal magnetic potential A_ϕ, (c) the normalised perturbation of the temperature, and (c) comparison of the peeling-ballooning mode growth rates with the reduced-MHD model, as a function of toroidal mode number.

This MAST benchmark is also run including the complete non-static equilibrium with flows and

Mach-1 boundary conditions. Figure-6 shows poloidal cross-sections of $n = 20$ perturbed quantities for the toroidal magnetic potential A_ϕ and the temperature (for the full-MHD model), together with the initial pedestal pressure gradient. The growth rates of the modes are plotted as a function of toroidal mode number and compared with reduced-MHD. The agreement between both models does not only show that the new full-MHD model behaves as expected, but also that reduced-MHD is capable of capturing the linear stability of peeling-ballooning modes for spherical tokamaks. As will be shown later in Section-4, the non-linear dynamics of ELM filaments is also very similar between reduced- and full-MHD.

Diamagnetic effects and neoclassical friction

The diamagnetic terms were tested using the X-point JET-like benchmark presented above. Figure-7a shows the growth rate with and without diamagnetic effects, as a function of toroidal mode number, for both reduced- and full-MHD. The agreement between the two models is reasonable, however it should be noted that the amplitude of the diamagnetic terms needed to be increased by 15% in order to obtain this match with reduced-MHD. Nevertheless, such a small deviation is within acceptable bounds.

(a)   (b)
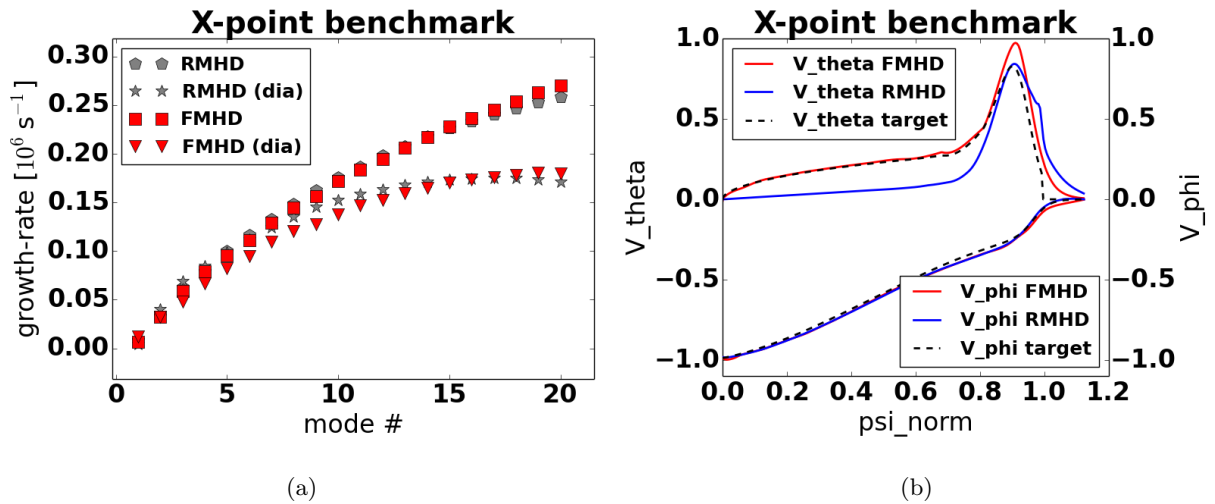
Figure 7:
Diamagnetic terms and neoclassical friction benchmark: (a) *The growth rate of the peeling-ballooning modes as a function of toroidal mode number n, with and without the diamagnetic effects, for both the reduced- and full-MHD models.* (b) *Toroidal and poloidal rotation profiles for a stationary kinetic X-point equilibrium. The two velocities are normalised and plotted positive and negative for clarity. The red lines are the full-MHD profiles, the blue ones are for the reduced-MHD, and the dashed-black lines are the target profiles, S_{NBI} and $|\vec{v}_{neo}|$.*

It is important to note that the diamagnetic terms from the induction equation-(12) can suffer from numerical fast-waves instabilities in some extreme cases. Although in the cases tested here, this issue does not occur at the physical amplitude of the diamgnetic effects, when trying to increase the amplitude beyond the physical value, fast-wave instabilities appear. It is possible that for some cases, particularly small devices with large diamagnetic amplitudes, numerical stabilisation, like Taylor-Galerkin [43] or Variational-Multiscale-Stabilisation [44] may be required.

The neoclassical friction terms, as well as toroidal momentum source, are tested using the same X-point case, to be compared against the reduced-MHD model. Figure-7b shows the comparison of velocity profiles in the toroidal and poloidal directions. This case is the same X-point JET-like plasma, run as a stationary axisymmetric kinetic equilibrium. For both the toroidal momentum and the neoclassical poloidal velocity, the full-MHD model is able to converge to the target prescribed profile. Note that both S_{NBI} and $\vec{v}_{neo}$ are prescribed only up to the separatrix.

Convergence and resolution

Convergence of growth rates as a function of spatial grid resolution is tested for the tearing and ballooning modes, using the tearing test-case described above, and the CBM18 ballooning case. The grid resolution is scanned homogeneously in the radial and poloidal directions, scanning from $(n_r, n_p){=}(27, 180)$ to $(90, 600)$, where n_r and n_p are the number of radial and poloidal grid-points, respectively (both equidistant in real-space). The error of the growth rates should scale inversely with the 5th power of the spatial resolution, as $(\sqrt{n_r n_p})^{-5}$. Although the tearing mode scales as expected, worse convergence is found for ballooning modes, such that the resolution required for full-MHD simulations is significantly higher than for reduced-MHD.
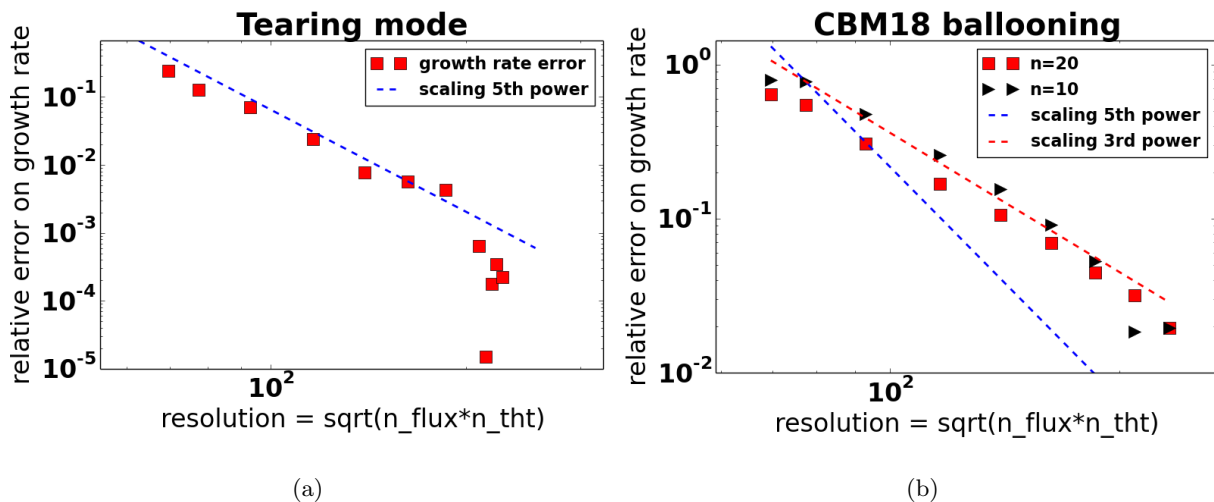
Figure 8:
The error of the growth rate is plotted as a function of the spatial resolution $\sqrt{n_r n_p}$ for (a) the tearing mode, and (b) the CBM18 ballooning mode. The error should converge as the 5th power of the spatial resolution, which is the case for the tearing mode, but not for ballooning modes. The reason for the lower convergence of ballooning modes is thought to be due to the interaction of fast-waves which require higher resolution at high β.

Figure-8 shows the convergence of the growth rate error, as a function of spatial resolution. For the tearing mode, the 5th order scaling is found as expected, and beyond a high enough resolution, the error diminishes dramatically, suggesting the growth rate is already fully converged. However, for ballooning modes using the CBM18 case, the growth rate convergence follows a scaling of the 3rd order. Unfortunately, the reason for this poorer convergence has not been elucidated yet. This lower scaling of ballooning instabilities seems to be similar for all toroidal mode numbers.

17

In practice, this means that a higher resolution is required for full-MHD simulations than for reduced-MHD to obtain the same error level. It should be noted that this scan has been achieved by scaling the spatial resolution homogeneously everywhere in the plasma, meaning that the same amount of spatial resolution is set for the core and the pedestal. In typical ELM simulations, however, since the mode is localised in the pedestal region, spatial resolution can be diminished in the core region and increased in the pedestal. This enables a reduction of the cost in radial resolution, but the poloidal resolution, however, needs to be elevated everywhere in the plasma, since ballooning modes span both the high- and low-field sides. The benchmark study presented above for ballooning modes was done at the highest resolution possible within the current capabilities of the code. At this level, using concentration of radial resolution at the pedestal, the error is negligible, below 1% of the growth-rate amplitude.

It should be noted that, unlike reduced-MHD, the convergence error for full-MHD is in the convenient direction, meaning that if the simulation is under-resolved, the instabilities are stabilised, whereas it is the opposite in reduced-MHD. Thus, artificial instabilities, which are possible in under-resolved reduced-MHD simulations, are avoided in full-MHD. Convergence tests should be performed for high-β cases to ensure growth rates are not affected in full-MHD.

4 Non-linear simulations

In this final section, we present three non-linear cases to demonstrate the ability of the model to address current open issues of tokamak MHD. These simulations are not meant to provide a validation against experiments, but rather to push the model into highly non-linear and unstable regimes, in order to test the numerical stability of the code. The three cases are an MGI-triggered disruption in JET, ELM filament dynamics in MAST, and an ELM crash in JET.

Core MHD and disruptions

The first non-linear case addressed here concerns core-MHD, where a disruption is triggered using the Massive-Gas-Injection method in a JET plasma. The JET experiment is chosen to be the pulse previously studied in [52, 53], discharge #86887. The simulation is run with toroidal mode numbers n=1,2,3,4,5, using a resistivity of η=1.5$\times$10$^{-6}\Omega.m$, and a viscosity of μ=1.5$\times$10^{-7}kg.m^{-1}.s^{-1}.

Since the full-MHD model does not yet include neutrals physics as in [52, 53], the MGI injection is mimicked by a density source S_{MGI} localised at the outer midplane of the plasma. Where the source is localised, a temperature sink is also introduced to account for the ionisation of the neutrals gas, such that T_{sink}=$-\xi S_{MGI}/2$, where ξ=13.6eV is the ionisation energy per neutral particle. The toroidally localised source is progressively displaced radially inward, starting from ψ_n=0.9 until ψ_n=0.6, spanning 4ms.

Of course, this is an extremely simplified and crude way to address MGI physics, but it should be emphasised again that the purpose of this simulation is not to reproduce the experiment exactly, but to trigger a non-linear crash and test the numerical reliability of the model. Future work will

Figure 9:

Simulation of an MGI-triggered disruption in JET. Columns from left to right: electron temperature T_e, electron density n_e, toroidal magnetic potential A_ϕ, and a Poincare plot of the magnetic field. Rows from top to bottom: time lapse of the simulation, at $t=0ms$, $t=2.8ms$, $t=4.2ms$, and $t=5.7ms$. Despite a very simplified MGI model lacking neutrals physics, core-MHD is triggered and a thermal-quench is obtained, demonstrating that the new full-MHD model is ready for advanced simulations of disruption physics without numerical issues.
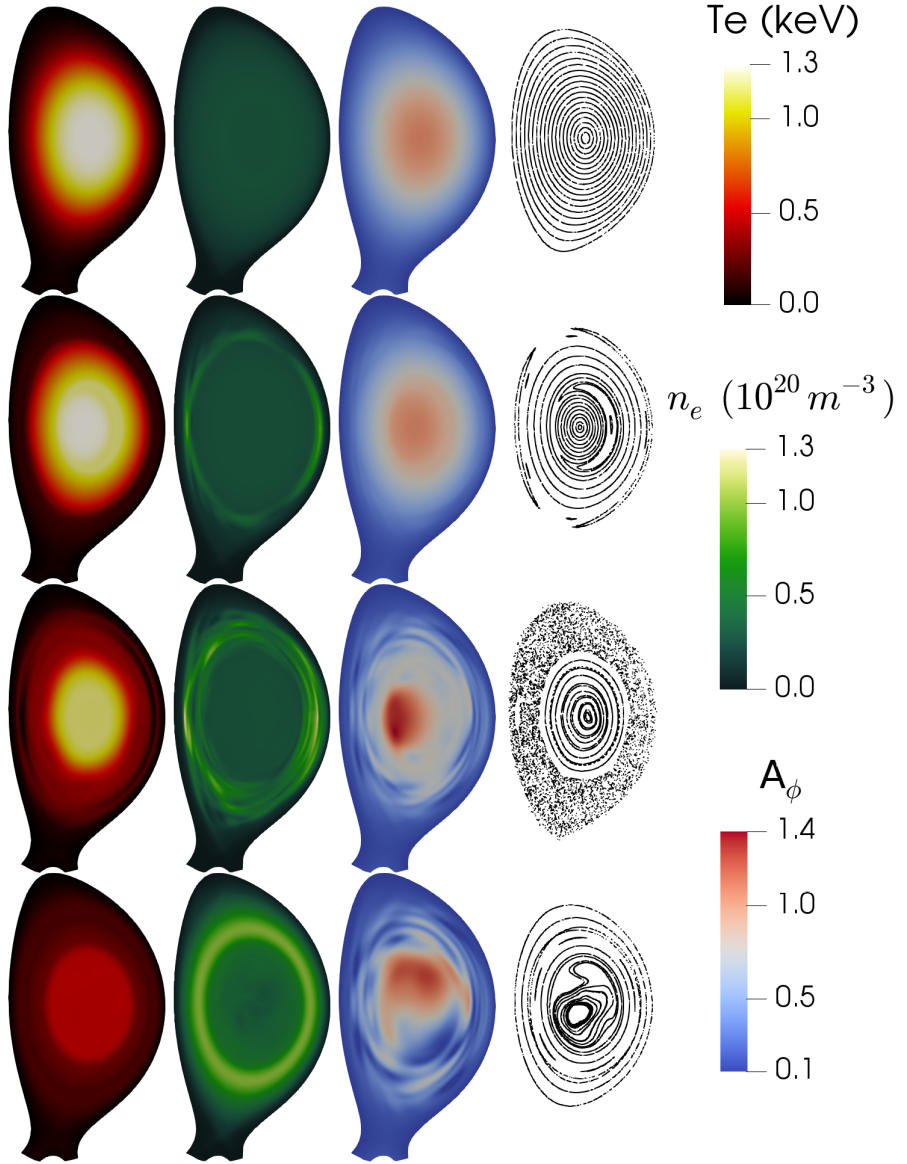
be dedicated to the inclusion of neutrals and impurity physics as in [52, 53], to address disruptions triggered by MGI as well as Shattered-Pellet-Injection (SPI). However, such additional ingredients are not expected to affect the numerical stability of the model, since neutrals and impurity physics enters the system of full-MHD only as a density source and a temperature sink (ie. in a similar manner as what was done here).

Figure-9 shows poloidal snapshots of the simulation as a function of time, for the variables T, ρ and A_ϕ, together with a Poincare plot of the magnetic field. The evolution of the MHD triggered by the localised density source is found to be the same as observations made in [53]. First, the $n=1$ mode becomes unstable in the core, later cascading to $n=2$ and higher mode numbers. The thermal quench occurs in two phases, firstly a loss of the outer layer of the plasma temperature through parallel conduction in a stochastic field region, and then through convective mixing in the core during the second phase. Thus, the non-linear dynamics of the modes seems to be well reproduced, including the formation of magnetic islands and stochastic regions. Most importantly,

the numerical stability of the model is well demonstrated, particularly considering that numerical hyper-resistivity and hyper-viscosity are not necessary here, unlike in the reduced-MHD version, where they are critically essential.

MAST SOL filament dynamics

Another demonstrative example of the ability of the new model to handle non-linear dynamics is an ELM instability in the MAST tokamak, for which filaments are observed to travel far into the SOL. As in previous reduced-MHD MAST studies [51, 54], the same dynamics is found with full-MHD, with filaments travelling radially at speeds of about 0.5-3km/s.
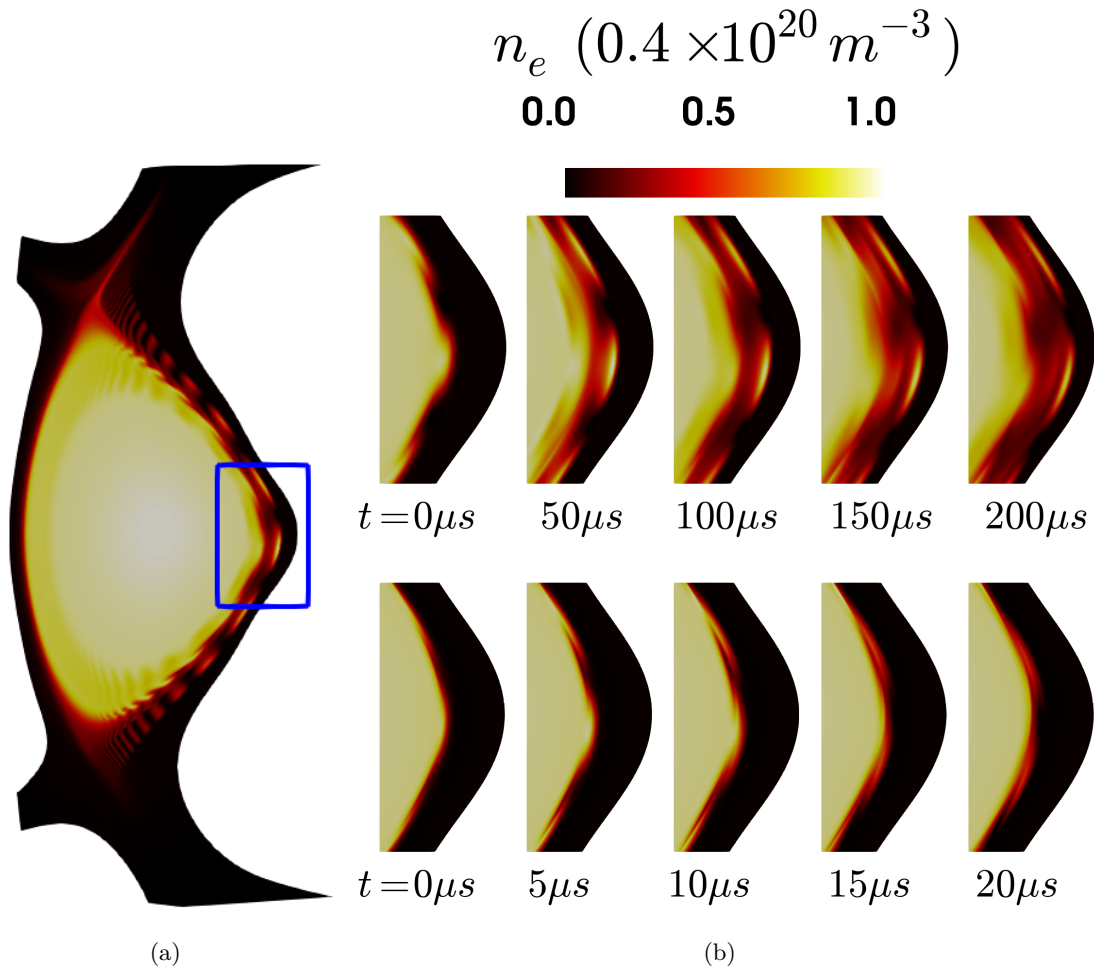
Figure 10:

Simulation of ELM filaments in the MAST tokamak, showing poloidal 2D-slices of plasma density. Filaments evolve radially at speeds in the range of 0.5-3km/s, depending on viscosity and resistivity. As resistivity increases, the resistive ballooning regime leads to larger growth-rates, and thus higher radial speeds. Viscosity, however, has a more complex effect. Low pedestal viscosity leads to higher growth-rates and higher initial filament speed, but low SOL viscosity leads to a strong shearing of filaments just after they cross the separatrix, as shown in the bottom case of (b). The top row of (b) shows a simulation with higher viscosity, where the filaments travel at a lower radial speed, but all the way into the far SOL. Plot (a) shows a poloidal snap-shot of the whole plasma, with the zoom-box inside which the slices of plot-(b) were obtained.

These simulations were performed using the ELMy H-mode pulse #24763 with the single mode number n=20, as in [51, 54]. One of the singular characteristics of filament dynamics in simulations

is that the radial speed and propagation of the filaments strongly depends on the SOL visco-resistive parameters. Particularly, as observed in [54], at very low SOL viscosity the filaments are sheared as they cross the separatrix, which stops their radial motion and leads to filaments travelling radially only up to a few `cm` in the SOL. More experimental behaviour is found at high SOL viscosity, where filaments are observed to travel at constant speed until the domain boundary, where Dirichlet boundary conditions stop the filament evolution.

Figure-10 shows poloidal snap-shots of the density in the MAST simulation, showing the time-evolution of filaments as they travel radially in the SOL. As filaments propagate radially, parallel transport convects/conducts plasma towards the target regions, resulting in filamentary lobes that are strongly sheared near the X-point due to the magnetic geometry of field lines. Two cases are plotted, using high viscosity (top row), and low viscosity (bottom row). Viscosity is observed to affect the evolution of filaments in the SOL. At lower viscosity, the initial growth rates of the ballooning modes are higher, resulting in a larger initial radial speed of filaments. However, this lower viscosity also results in a strong shearing of the filaments, which aborts the evolution of the filaments just outside the separatrix. At higher viscosity (top-row), the filaments travel at a lower speed, but at constant velocity all the way into the far SOL. The same behaviour was observed in [54], so it is concluded that reduced- and full-MHD are in good agreement, both for the linear stability and the non-linear dynamics of SOL filaments in spherical tokamaks like MAST.

Future works on MAST and MAST-U could contribute to the study of ELM burn-through [55], core-MHD and disruption studies, and the exploration of viscous models to describe accurately the evolution of SOL filaments. These will require further developments of the model, particularly the inclusion of neutrals physics, which is not addressed in this work.

JET ELM simulation

Finally, the new model's capability to handle strongly non-linear MHD instabilities is illustrated with an ELM simulation in the JET tokamak, using multiple mode numbers and diamagnetic effects. The resistivity is taken to be a factor 20 above the experimental neoclassical amplitude. For ELM simulations at experimental resistivity, it is now understood that the temporal evolution of the pedestal build-up is needed, leading up to the ELM onset [56, 57]. As demonstrated in [56, 57], non-linear ELM onsets have an explosive behaviour which leads to larger ELM crashes than a simulation started from a linearly unstable pre-ELM state. Such simulations, however, require long computation times and detailed set-up, which will be addressed with full-MHD in future work.

The JET pulse used for this simulation is a well-studied ELMy H-mode experiment, #83334, which was studied in [56, 58, 59]. The simulation is performed using the toroidal mode numbers n=1,2,3,...,10. The pedestal losses obtained here are 21% for density and 23% for temperature (relative the pedestal content, integrated in the range ψ_n=[0.85 − 1.0]). The mode n=5 begins the crash, until other modes start interacting in the later phase of the ELM.
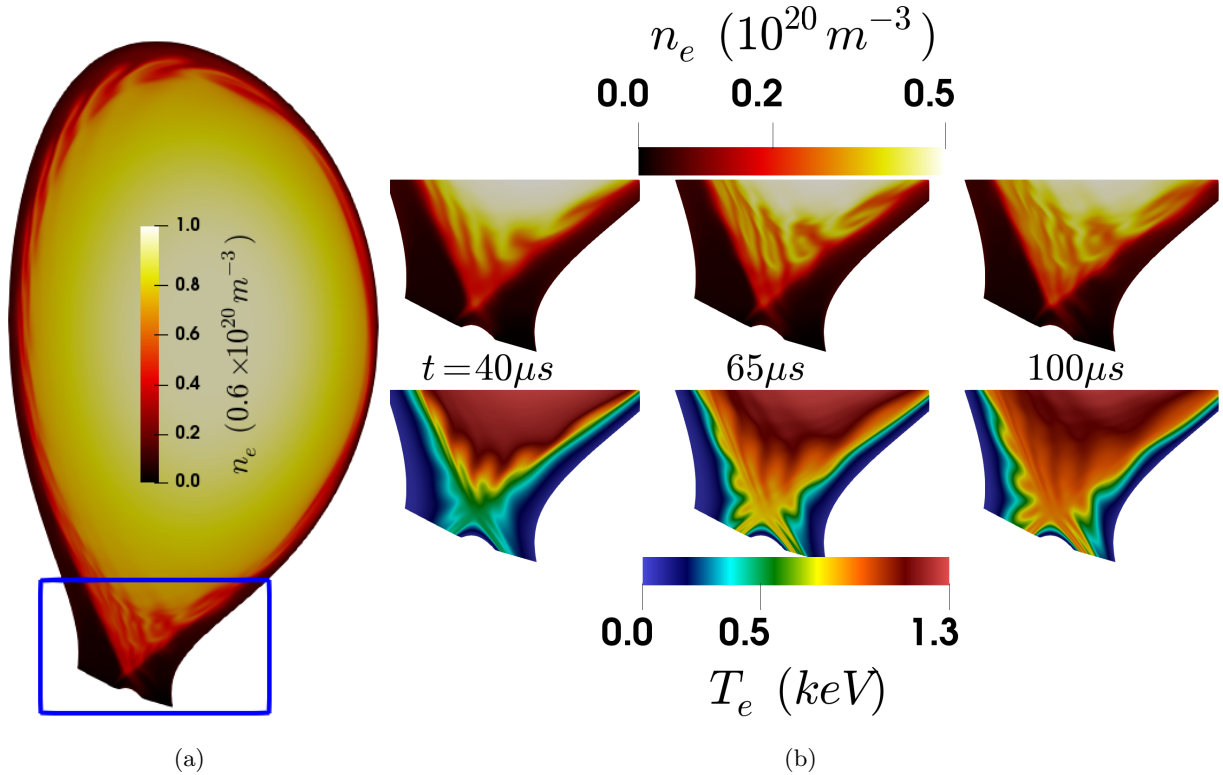
Figure 11:
Simulation of an ELM in the JET tokamak, showing poloidal 2D-slices of plasma density and temperature, as a function of time. The conduction of temperature along magnetic field lines forms lobes structures that result in footprints on the divertor targets, similar to what is observed in reduced-MHD simulations. The density filaments, however, result in eddies inside the pedestal, which was not observed in reduced-MHD. The blue box in plot-(a) shows the zoom area used for the slices of plot-(b).

One intriguing observation made from ELM simulations with the full-MHD model is the clear formation of swirling eddies inside the pedestal as filaments leave the plasma, as shown in Figure-11. Such eddies were never observed in reduced-MHD simulations, suggesting that the restriction of formulating $\vec{v}_\perp$ as a function of a scalar electric potential may play a role in filament convection. However, it is not yet clear whether such differences play any role in global aspects of simulations, where quantitative comparisons of integrated measurements (like ELM size and divertor heat-fluxes) would need to be performed for multiple pulses, as in [56, 58].

Detailed studies of ELM physics using the full-MHD model will be required in the near future to provide extensive validation of the model against experiments. Such studies are now possible, and the non-linear simulations presented here clearly show that the model is numerically sound and ready for such extensive studies.

5   Summary and future works

This paper presents the significant advancement of MHD simulations using the JOREK code, with the inclusion of a full-MHD model. The model was described in details, including extended MHD terms like momentum sources and diamagnetic effects. Linear benchmark of the new model was

performed against the previously studied reduced-MHD model, showing satisfactory agreement. Linear tests were performed for core-MHD circular plasmas as well as ballooning modes in circular and X-point plasmas, including diamagnetic effects. Additionally, a spherical plasma was tested using MAST experimental data, showing that reduced- and full-MHD are in good agreement, even for small aspect-ratio machines like MAST. It has long been asserted that reduced-MHD is unable to describe accurately the physics of MHD instabilities in spherical plasmas, and this paper demonstrates that it is indeed not the case. Finally, non-linear simulations were performed for a disruption in a JET plasma, for the dynamic evolution of SOL filaments during ELMs in the MAST tokamak, and for a non-linear ELM crash in a JET plasma, showing all the key characteristics expected from previous studies with the reduced-MHD model.

Beyond the demonstration that the new full-MHD model is reliable with respect to physics aspects of MHD instabilities, this paper also demonstrates the remarkable numerical stability of the model. Although numerical stabilisation is often required to avoid issues resulting from fast-waves inherent to full-MHD, the simulations presented above demonstrate that no such stabilisation is required for many of the experimentally relevant MHD instabilities in tokamak plasmas. It may be expected that in some extreme regimes, such stabilisation could be required, and future works should aim at implementing stabilisation methods like Taylor-Galerkin (TG) or Variational-Multi-Scale (VMS) methods [43, 44].

As such, the new full-MHD model is now ready for full production and quantitative validation against experiments. Of course, further developments of the model will now be required in the near future to address specific tokamak instabilities like disruptions, detachment and ELM burn-through, which requires neutrals and impurity physics. However, it is not expected that these additional physics effects will deteriorate the numerical stability of the model, since they enter the system as terms that were already included and tested here (mainly density sources and temperature sinks). Another important aspect of future developments will be to address more elaborate boundary conditions, with wall-extended grids as in [59], and coupling with the free-boundary model STARWALL, as in [42, 60].

Acknowledgement

Data Availability

Data for figures and tables is available online, under the DOI 10.5281/zenodo.3894111, titled "Extended Full-MHD Simulation of Non-linearInstabilities in Tokamak Plasmas":

    https://doi.org/10.5281/zenodo.3894111

References

[1] T. Eich, A. Herrmann, and J. Neuhauser. *Phys. Rev. Lett. 91, 195003*, 2003.

[2] B Sieglin, M Faitsch, T Eich, A Herrmann, and W Suttrop. *Physica Scripta 2017, T170*, 2017.

[3] C Ham, A Kirk, S Pamela, and H Wilson. *Nature Rev. Phys. 2, 159-167*, 2020.

[4] A.W.Leonard. *Phys. Plasmas 21, 090501.*, 2014.

[5] C.Cheng, L Chen, and M S Chance. *Ann. Phys. 161, 21*, 1985.

[6] A.Dvornova, G. T. A. Huijsmans, S. Sharapov, F. J. Artola Such, P. Puglia, M. Hoelzl, S. Pamela, A. Fasoli, and D. Testa. *Phys. Plasmas 27, 012507.*, 2020.

[7] M.Fitzgerald, J.Buchanan, R.J.Akers, B.N.Breizman, and S.E.Sharapov. *Comp. Phys. Comm. 252, 106773*, 2020.

[8] S. D. Pinches, I. T. Chapman, Ph. W. Lauber, H. J. C. Oliver, S. E. Sharapov, K. Shinohara, and K. Tani. *Phys. Plasmas 22, 021807*, 2015.

[9] A.H.Boozer. *Phys. Plasmas 19, 058101*, 2012.

[10] P. C. de Vries, G. Pautasso, D. Humphreys, M. Lehnen, S. Maruyama, J. A. Snipes, A. Vergara, and L. Zabeo. *Fus. Sci. Technol. 69, 471-484*, 2016.

[11] M.Lehnen, K.Aleynikova, P.B.Aleynikov, D.J.Campbell, P.Drewelow, N.W.Eidietis, Yu.Gasparyan, R.S.Granetz, Y.Gribov, N.Hartmann, E.M.Hollmann, and V.A.Izzo et al. *J. Nucl. Mater. 463, 39-48*, 2015.

[12] F. J. Artola, K. Lackner, G. T. A. Huijsmans, M. Hoelzl, E. Nardon, , and A. Loarte. *Phys. Plasmas 27, 032501*, 2020.

[13] D. Hu, E. Nardon, M. Lehnen, G.T.A. Huijsmans, and D.C. van Vugt. *Nucl. Fusion 58, 12*, 2018.

[14] V. Bandaru, M. Hoelzl, F. J. Artola, G. Papp, and G. T. A. Huijsmans. *Phys. Rev. E 99, 063317*, 2019.

[15] JOREK. *https://www.jorek.eu/*, 2020.

[16] G.T.A.Huysmans and O.Czarny. *Nucl. Fusion 47, 659*, 2007.

[17] M3D-C1. *https://w3.pppl.gov/ nferraro/m3dc1.html*, 2020.

[18] S.C.Jardin. *J. Comp. Phys. 200-133*, 2004.

[19] NIMROD. *https://nimrodteam.org/*, 2020.

[20] C.R.Sovinec, A.H.Glasser, T.A.Gianakon, D.C.Barnes, R.A.Nebel, S.E.Kruger, D.D.Schnack, S.J.Plimpton, A.Tarditi, M.S.Chufth, and the NIMROD Team. *J Comp. Phys. 195, 355*, 2004.

[21] H.Lutjens and JF Luciani. *J Comp. Phys. 227, 14, 6944-6966*, 2008.

[22] BOUT++. *https://boutproject.github.io/*, 2020.

[23] B.D.Dudson, M.V.Umansky, X.Q.Xu, P.B.Snyder, and H.R.Wilson. *Comp. Phys. Comm. 180, 1467-1480*, 2009.

[24] Y.Todo. *New Journal Phys. 18*, 2016.

[25] A. Konies, S. Briguglio, N. Gorelenkov, T. Feher, M. Isaev, Ph. Lauber, A. Mishchenko, D.A. Spong, Y. Todo, W.A. Cooper, R. Hatzky, R. Kleiber, M. Borchardt, G. Vlad, A. Biancalani, and A. Bottino. *Nucl. Fusion 58, 12*, 2018.

[26] H.R. Strauss. *Phys. Fluids 19, 134*, 1976.

[27] H.R. Strauss. *J. Plasma Physics, Vol. 57, part 1, pp 83-87*, 1997.

[28] J P Graves, D Zullino, D Brunetti, S Lanthaler, and C Wahlberg. *Plasma Phys. Contr. Fusion 61, 10, 104003*, 2019.

[29] J.W.Haverkort, H.J.de Blank, G.T.A.Huysmans, J.Pratt, and B.Koren. *J Comp. Phys. 316, 281-302*, 2016.

[30] I T Chapman, N R Walkden, J P Graves, and C Wahlberg. *Plasma Phys. Control. Fusion 53, 12*, 2011.

[31] R.D.Hazeltine and J.D.Meiss. *Plasma Confinement, Redwood City: Addison-Wesley Publishing Company*, 1992.

[32] B.N.Rogers and J. F. Drake. *Phys. Plasmas 6-7, 2797*, 1999.

[33] R.J.Hastie, P.J. Catto, and J. J. Ramos. *Phys. Plasmas 7-11, 4561*, 2000.

[34] F. Orain, M. Becoulet, G. Dif-Pradalier, G. Huijsmans, S. Pamela, E. Nardon, C. Passeron, G. Latu, V. Grandgirard, A. Fil, A. Ratnani, I. Chapman, A. Kirk, A. Thornton, M. Hoelzl, and P. Cahyna. *Phys. Plasmas 20, 102510*, 2013.

[35] D. D. Schnack, D. C. Barnes, D. P. Brennan, C. C. Hegna, E. Held, C. C. Kim, S. E. Kruger, A. Y. Pankin, and C. R. Sovinec. *Phys. Plasmas 13, 058103*, 2006.

[36] D. D. Schnack, J. Cheng, D. C. Barnes, and S. E. Parker. *Phys. Plasmas 20, 062106*, 2013.

[37] O. Fevrier, T. Nicolas, P. Maget, J.H. Ahn, X. Garbet, and H. Lutjens. *Nucl. Fusion 58 096008*, 2018.

[38] M. Becoulet, M. Kim, G. Yun, S. Pamela, J. Morales, X. Garbet, G.T.A. Huijsmans, C. Passeron, O. Fevrier, M. Hoelzl, A. Lessig, and F. Orain. *Nucl. Fusion 57, 116059*, 2017.

[39] J.J.Ramos. *Phys. Plasmas 12, 112301*, 2005.

[40] O.Czarny and G.T.A.Huysmans. *J. Computational Phys. 227, 7423*, 2008.

[41] J.G.Watkins, T.E.Evans, M.Jakubowski, R.A.Moyer, O.Schmitz, A.Wingen, M.E.Fenstermacher, I.Joseph, C.J.Lasnier, and D.L.Rudakov. *J Nucl. Mat. 390-391, 839-842*, 2009.

[42] M Hoelzl, P Merkel, G T A Huysmans, E Nardon, E Strumberger, R McAdams, I Chapman, S Gunter, and K Lackner. *Journal of Physics: Conference Series 401, 012010*, 2012.

[43] J.Donea, L.Quartapelle, and V.Selmin. *J Comp. Phys., 70(2), 463-499*, 1987.

[44] J.P.Trelles and S.M.Modirkhazeni. *Comp. Methods Applied Mech. Engin., 282(0), 87-131*, 2014.

[45] H.Guillard. *https://hal.inria.fr/hal-01145009/document*, 2015.

[46] E.Franck M Hoelzl, A Lessig, and E Sonnendrucker. *ESAIM:M2AN 49, 5, https://doi.org/10.1051/m2an/2015014*, 2015.

[47] G.T.A. Huysmans and J. P. Goedbloed. *Phys. Fluids B 5, 1545*, 1993.

[48] E.Strumberger S. Gunter. *Nucl. Fusion 57(1), 016032*, 2017.

[49] A.B. Mikhailovskii, G.T.A. Huysmans, W.O.K. Kerner, and S.E. Sharapov. *Plasma Phys. Rep. 23 844*, 1997.

[50] G.T.A. Huysmans, S. E. Sharapov, A. B. Mikhailovskii, and W. Kerner. *Phys. Plasmas 8, 4292*, 2001.

[51] S J P Pamela, G T A Huijsmans, A Kirk, I T Chapman, J R Harrison, R Scannell, A J Thornton, M Becoulet, and F Orain. *Plasma Phys. Control. Fusion 55, 095001*, 2013.

[52] A. Fil, E. Nardon, M. Hoelzl, G. T. A Huijsmans, F. Orain, M. Becoulet, P. Beyer, G. Dif-Pradalier, R. Guirlet, H. R. Koslowski, M. Lehnen, J. Morales, S. Pamela, C. Passeron, C. Reux, and F. Saint-Laurent. *Physics of Plasmas 22, 062509*, 2015.

[53] E Nardon, A Fil, M Hoelzl, and G Huijsmans. *Plasma Phys. Control. Fusion 59, 014006*, 2017.

[54] S.Pamela, G.Huijsmans, A.Kirk, and I.Chapman. *41st EPS Conf. P5.061, http://ocs.ciemat.es/EPS2014PAP/pdf/P5.061.pdf*, 2014.

[55] S.F. Smith, S.J.P. Pamela, A. Fil, M. Hoelzl, G.T.A. Huijsmans, A. Kirk, D. Moulton, O. Myatra, A.J. Thornton, and H.R. Wilson. *Nucl. Fusion 60, 066021*, 2020.

[56] S.J.P. Pamela, G.T.A. Huijsmans, T. Eich, S. Saarelma, I. Lupelli, C.F. Maggi, C. Giroud, I.T. Chapman, S.F. Smith, L. Frassinetti, M. Becoulet, M. Hoelzl, F. Orain, and S. Futatani. *Nucl. Fusion 57, 076006*, 2017.

[57] A.Cathey et al. *Phys. Rev. Lett. (submitted)*, 2020.

[58] S Pamela, T Eich, L Frassinetti, B Sieglin, S Saarelma, G Huijsmans, M Hoelzl, M Becoulet, F Orain, S Devaux, I Chapman, I Lupelli, and E Solano. *Plasma Phys. Control. Fusion 58, 014026*, 2015.

[59] S.Pamela, G.Huijsmans, A.J.Thornton, A.Kirk, S.F.Smith, M.Hoelzl, and T.Eich. *Comp. Phys. Comm. 243, 41-50*, 2019.

[60] F.J. Artola, G.T.A. Huijsmans, M. Hoelzl, P. Beyer, A. Loarte, and Y. Gribov. *Nucl. Fusion 58, 096018*, 2018.